

See discussions, stats, and author profiles for this publication at: <https://www.researchgate.net/publication/277086750>

# Co<sub>2</sub>(OH)<sub>2</sub>CO<sub>3</sub> Nanosheets and CoO Nanonets with Tailored Pore Sizes as Anodes for Lithium Ion Batteries

ARTICLE in ACS APPLIED MATERIALS & INTERFACES · MAY 2015

Impact Factor: 6.72 · DOI: 10.1021/acsaami.5b02152 · Source: PubMed

---

CITATIONS

3

READS

67

## 6 AUTHORS, INCLUDING:



Zhou Xianlong

Nankai University

20 PUBLICATIONS 127 CITATIONS

[SEE PROFILE](#)



Yiren Zhong

Yale University

19 PUBLICATIONS 185 CITATIONS

[SEE PROFILE](#)



Mei Yang

Nanjing University of Science and Technology

18 PUBLICATIONS 227 CITATIONS

[SEE PROFILE](#)



Zhen Zhou

Nankai University

213 PUBLICATIONS 6,993 CITATIONS

[SEE PROFILE](#)

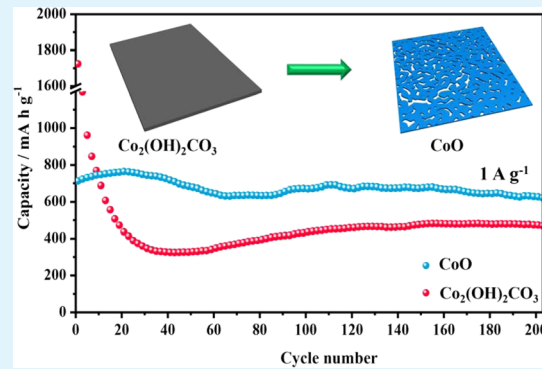
# Co<sub>2</sub>(OH)<sub>2</sub>CO<sub>3</sub> Nanosheets and CoO Nanonets with Tailored Pore Sizes as Anodes for Lithium Ion Batteries

Xianlong Zhou, Yiren Zhong, Mei Yang, Qiang Zhang, Jinping Wei, and Zhen Zhou\*

Tianjin Key Laboratory of Metal and Molecule Based Material Chemistry, Key Laboratory of Advanced Energy Materials Chemistry (Ministry of Education), Institute of New Energy Material Chemistry, School of Materials Science and Engineering, Collaborative Innovation Center of Chemical Science and Engineering (Tianjin), Nankai University, Tianjin 300071, China

## S Supporting Information

**ABSTRACT:** Co<sub>2</sub>(OH)<sub>2</sub>CO<sub>3</sub> nanosheets were prepared and initially tested as anode materials for Li ion batteries. Benefiting from hydroxide and carbonate, the as-prepared sample delivered a high reversible capacity of 800 mAh g<sup>-1</sup> after 200 cycles at 200 mA g<sup>-1</sup> and long-cycling capability of 400 mAh g<sup>-1</sup> even at 1 A g<sup>-1</sup>. Annealed in Ar, monoclinic Co<sub>2</sub>(OH)<sub>2</sub>CO<sub>3</sub> nanosheets were transformed into cubic CoO nanonets with rich pores. The pore size had apparent influence on the high-rate performances of CoO. CoO with appropriate pore sizes exhibited greatly enhanced Li storage performances, stable capacity of 637 mAh g<sup>-1</sup> until 200 cycles at 1 A g<sup>-1</sup>. More importantly, after many fast charge–discharge cycles, the highly porous nanonets were still maintained. Our results indicate that Co<sub>2</sub>(OH)<sub>2</sub>CO<sub>3</sub> nanosheets and highly porous CoO nanonets are both promising candidate anode materials for high-performance Li ion batteries.



**KEYWORDS:** Co<sub>2</sub>(OH)<sub>2</sub>CO<sub>3</sub>, CoO nanonets, Pore size, Li ion batteries, anode materials

## INTRODUCTION

Nowadays, lithium-ion batteries (LIBs) have conquered the market of portable electronics, because of their high energy density, longevity, and environmental benignity. However, the commercial graphite anode displays a relatively low theoretical capacity (372 mAh g<sup>-1</sup>).<sup>1</sup> For the successful launch of electric vehicles and smart grids, LIBs must be further developed to improve their power and energy density without sacrificing the safety and cost.<sup>2,3</sup> Therefore, it is of critical importance to explore novel high-performance anode materials for next-generation LIBs.

CoO, a typical transition-metal oxide, was first reported as an anode material for LIBs in 2000.<sup>4</sup> Since then, it has been widely considered as an attractive anode material, because of its high theoretical capacity and easy preparation.<sup>5</sup> Nevertheless, the actual performance of CoO is seriously impeded by its intrinsic drawback, namely, low conductivity and large volume changes (246%) upon cycling. In order to overcome these barriers, many appealing strategies have been adopted to ameliorate the electrochemical performances of CoO. One typical approach is to add highly electrically conductive materials to form the composites. In this scenario, various CoO composites with graphene,<sup>6–8</sup> nitrogen-doped carbon,<sup>9</sup> and carbon nanofibers<sup>10,11</sup> have been successfully prepared. Although they delivered high reversible capacity, the inclusion of too much carbon sacrifices the specific capacity of the CoO electrode.<sup>12</sup> The other is rationally designing and preparing CoO with different morphologies and desired nanostructures, such as

octahedral nanocages,<sup>13</sup> highly ordered nanosheets,<sup>14</sup> and metasequoia,<sup>15</sup> as well as directionally fabricating mesopore structure.<sup>16</sup> Both can effectively enlarge the surface-to-volume ratio and reduce diffusion distance for Li<sup>+</sup>, favorably allowing better reaction kinetics at the electrode surface and significantly preventing electrode polarization. Simultaneously, the pore size imposes effects on the electrochemical performances of electrodes.<sup>17,18</sup> However, so far, there is still a lack of understanding of the relationship between the pore size and volume change for CoO. In fact, the porosity contributes to alleviate volume changes, but the expansion cannot exceed the room offered by the pores. Typically, undersized pores cannot provide enough space to accommodate the huge change, resulting in the breakdown of materials and the loss of electrical contact, eventually leading to capacity fading upon cycling.<sup>8</sup> In contrast, pores that are too large cause the bending of nanosheets during cycling, which influences the cycling efficiency of batteries.<sup>19</sup> From this point of view, the optimum pore size is a key to obtain cycling stability for electrode materials. However, so far, there are rare studies on high capacity carbon-free CoO with size-controlled pores for LIBs. Note that “carbon-free” here only covers the stage of material preparation, and during the electrode preparation, extrinsic electrically conductive carbon materials are still needed.

Received: March 11, 2015

Accepted: May 19, 2015

Published: May 19, 2015



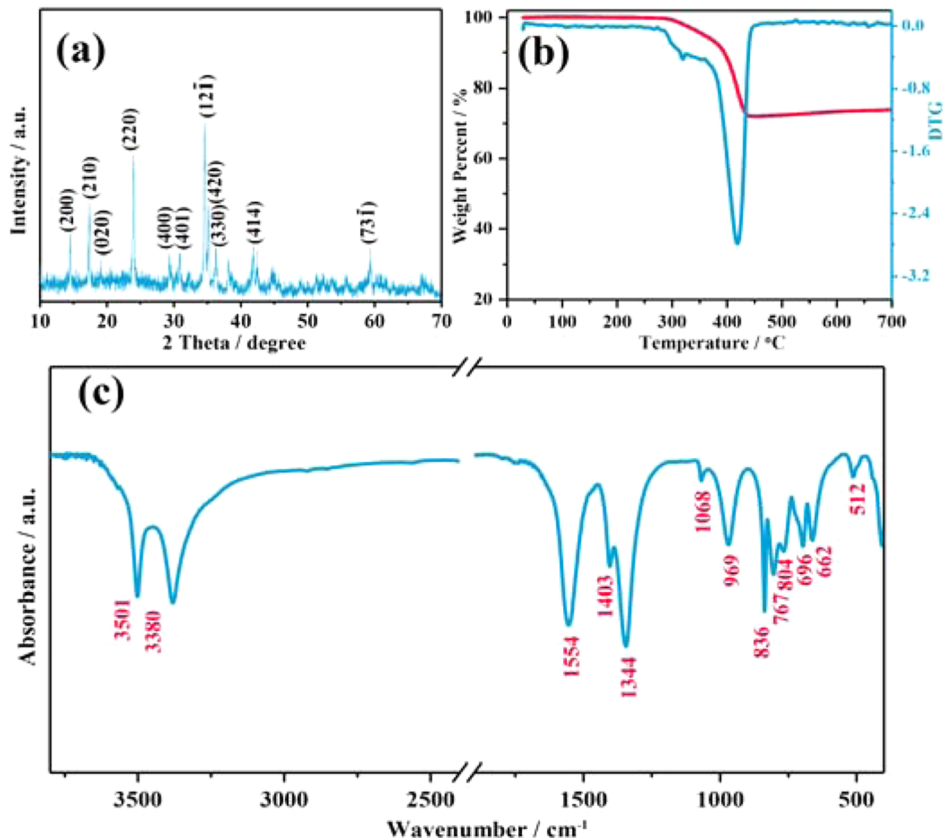


**Figure 1.** (a) XRD patterns, (b) TGA curve, and (c) FTIR for  $\text{Co}_2(\text{OH})_2\text{CO}_3$ .

Nanostructured CoO is generally obtained via a two-step approach, where Co-based intermediate compounds, such as  $\text{Co}(\text{OH})_2$ ,<sup>8</sup>  $\text{CoCO}_3$ ,<sup>20,21</sup> and  $\text{Co}(\text{CO}_3)_{0.5}(\text{OH}) \cdot 11\text{H}_2\text{O}$ ,<sup>16</sup> are first prepared and followed by subsequent calcination. Note that both  $\text{Co}(\text{OH})_2$  and  $\text{CoCO}_3$  have been studied in recent years as promising anode materials for LIBs. For example,  $\text{Co}(\text{OH})_2$  nanosheet-graphene composites, prepared by He et al., exhibited high lithium storage capacity (as large as 1120 mAh g<sup>-1</sup>);<sup>22</sup> Su et al. reported that  $\text{CoCO}_3$  submicrocube-graphene composites delivered specific capacities over 1000 mAh g<sup>-1</sup>.<sup>23</sup> Apparently, both displayed additional reversible capacity beyond their theoretical values based on conversion reactions. The extra capacity is mainly due to the contribution of LiOH or  $\text{Li}_2\text{CO}_3$  upon cycling.<sup>23–26</sup> However, metal hydroxycarbonates have never been touched as LIB anode materials, although  $\text{Ni}_2(\text{OH})_2\text{CO}_3$  was reported as a promising material for supercapacitors.<sup>27</sup>

In this work, we prepared  $\text{Co}_2(\text{OH})_2\text{CO}_3$  nanosheets via a hydrothermal route, and first investigated them as anode materials for LIBs. To further enhance the performance at large current densities,  $\text{Co}_2(\text{OH})_2\text{CO}_3$  nanosheets were then converted to highly porous CoO nanonets by subsequent calcination in Ar. By turning the pore size, the nanosheets offered enough space for accommodating the volume variation and alleviating the structural strain associated with repeated lithiation and delithiation. Hence, carbon-free CoO nanosheets with hierarchical porous structure exhibited further enhanced Li storage performances.

## EXPERIMENTAL SECTION

**Material Preparation.** All reagents were of analytic grade and were used without further purification. Cobaltous nitrate (3 mmol) and 3.0 g of urea were dispersed in 70 mL of deionized water with strong agitation for 20 min. The mixed solutions were transferred into a 100 mL Teflon-lined autoclave, heated at 180 °C for 3 h, and then cooled to room temperature naturally. The  $\text{Co}_2(\text{OH})_2\text{CO}_3$  precipitate was centrifuged and washed with water and ethanol for at least three times separately, and dried at 60 °C for 12 h. Various CoO nanosheets were prepared by heating the as-prepared  $\text{Co}_2(\text{OH})_2\text{CO}_3$  at 500 °C in an Ar atmosphere for different times, followed by a natural cooling process to room temperature. The heating rates were all set at 5 °C min<sup>-1</sup>.

**Material Characterization.** The as-prepared samples were characterized by X-ray diffraction (XRD, Rigaku D/MAX III diffractometer with Cu K $\alpha$  radiation,  $\lambda = 1.5418 \text{ \AA}$ ) and field-emission scanning electron microscope (FESEM, Hitachi S-3500N). Transmission electron microscope (TEM), selected area electron diffraction (SAED), and high-resolution TEM (HRTEM) were taken on a FEI Tecnai G2F-20. Fourier transform infrared (FTIR) spectroscopy was performed on Nicolet MAGNA-560 FTIR spectrometer by using KBr pellets. Elemental analyses (C and H) were performed on a Perkin–Elmer 240C analyzer. Thermogravimetric analysis (TGA) was conducted in air by using PTC-10A TG-DTA analyzer from room temperature to 700 °C with a heating rate of 10 °C min<sup>-1</sup>. The specific surface area and porosity of the sample were measured by N<sub>2</sub> adsorption–desorption technique (Quantachrome NovaWin).

**Electrochemical Tests.** In test cells, lithium metal was used as the counter and reference electrode. The working electrodes were composed of the active material, polyvinylidene fluoride (PVDF), and acetylene black with the weight ratio of 75:15:10. The electrode was prepared by casting the slurry onto copper foil with a doctor blade and drying in a vacuum oven at 110 °C for 12 h. The average weight of the working electrodes was 1.0–1.2 mg. The electrolyte was 1 mol L<sup>-1</sup>

$\text{LiPF}_6$  dissolved in a dimethyl carbonate (DMC)/ethyl methyl carbonate (EMC)/ethylene carbonate (EC) mixture (1:1:1 v/v/v), while Celgard 2400 membrane was used as a separator. The cells were assembled in a glovebox filled with high-purity argon. Charge/discharge measurements were performed between the potential range of 0.01 and 3.00 V (vs Li/Li<sup>+</sup>) under a LAND-CT2001A instrument at 25 °C. Cyclic voltammetry (CV) was performed at a scanning rate of 0.1 mV s<sup>-1</sup> between 0.01 and 3.00 V at 25 °C.

## RESULTS AND DISCUSSION

**Characterization and Electrochemical Performance of  $\text{Co}_2(\text{OH})_2\text{CO}_3$  Nanosheets.** The crystalline nature and phase purity of the prepared products were ascertained by XRD patterns in Figure 1a. All the diffraction peaks can be perfectly indexed to monoclinic cobalt hydroxycarbonate, which is consistent with the previous report,<sup>28</sup> including the peak position and intensity. The sample adopts  $P21/a$  (No. 14) space group and yields lattice parameters of  $a = 12.886(6)$  Å,  $b = 9.346(3)$  Å,  $c = 3.156(1)$  Å, and  $\beta = 110.358(6)$ °. In order to confirm no interlayer water molecules in it, TGA and elemental analysis were further executed. In Figure 1b, there is no change for the sample below 300 °C. However, when the temperature increases to 700 °C, the total weight loss is ~28.0%, because of the simultaneous removal of hydroxyl and carbonate anions, very close to the theoretical value. Moreover, the result was confirmed by the elemental analysis (Table S1 in the Supporting Information), and the weight percentage of carbon and hydrogen tallies with the theoretical value. Besides, the compositions of the sample were further investigated through FTIR spectroscopy (Figure 1c). Notably, the strong peaks at  $\sim 3501$  cm<sup>-1</sup> is assigned to the stretching vibration of the O–H bond, indicative of the presence of hydroxyl ions due to the metal–OH layer, while the interaction between O–H groups and carbonate anions can also be found at 3380 cm<sup>-1</sup>.<sup>29</sup> From middle to lower wave numbers, the presence of  $\text{CO}_3^{2-}$  in the sample is evidenced by its vibration bands, which suggests the presence of monodentate or polydentate carbonate ligands.<sup>30</sup> The peaks observed at 1554, 1403, 1344, 1068, 836, 767, and 696 cm<sup>-1</sup> are ascribed to  $\nu(\text{OCO}_2)$ ,  $\nu(\text{CO}_3)$ , C–O,  $\nu(\text{C}=\text{O})$ ,  $\delta(\text{CO}_3)$ ,  $\delta(\text{OCO})$ , and  $\rho(\text{OCO})$ , respectively.<sup>29,30</sup> The other two characteristic bands at 969 and 512 cm<sup>-1</sup> are indicative of (Co–OH) bending modes and  $\rho_w$  (Co–OH).<sup>31</sup> Collectively, XRD, TGA, elemental analysis, and FTIR together demonstrate that the hydrothermally prepared product is  $\text{Co}_2(\text{OH})_2\text{CO}_3$ .

The microstructure of the as-prepared sample was characterized by using FESEM and TEM. The bulk nanosheets can be directly observed in Figure 2a; these large-size structures are very consistent with the sharp peaks of XRD. As illustrated in Figure 2b, similar rectangular nanosheets can be observed. High crystallization can be visualized through the HRTEM image (Figure 2c), which is taken from the red square region in Figure 2b. The clear lattice fringes in two regions can be seen obviously with  $d$ -spacings of 0.25 and 0.46 nm, readily indexed to the (020) and (420) planes of  $\text{Co}_2(\text{OH})_2\text{CO}_3$ , respectively. Besides, the corresponding fast Fourier transform (FFT) pattern is collected in Figure 2d, which indicates the nature of monoclinic  $\text{Co}_2(\text{OH})_2\text{CO}_3$ . Simultaneously, the diffraction spots are assigned to the (020), (420), and (400) planes, respectively, which also coincide with the above XRD results. Moreover, the SAED (inset of Figure 2c) clearly reveals the single-crystalline nature of the  $\text{Co}_2(\text{OH})_2\text{CO}_3$  sample.

The electrochemical performances of  $\text{Co}_2(\text{OH})_2\text{CO}_3$  were tested as LIB anodes in detail. To begin with, the reactions

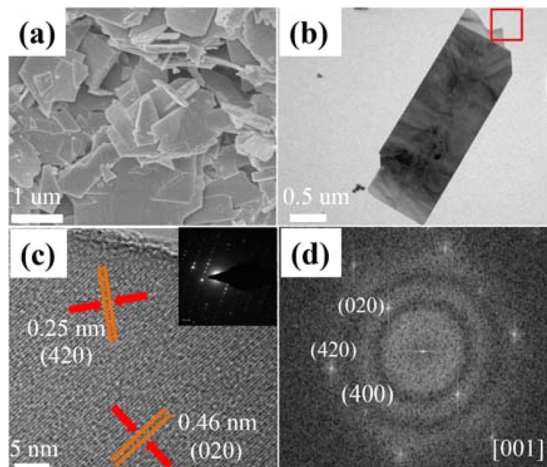
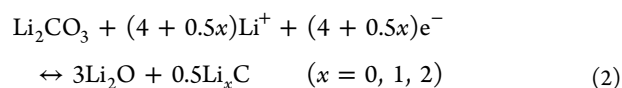
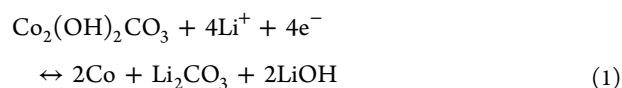


**Figure 2.** (a) FESEM, (b) TEM, (c) HRTEM images as well as SAED (shown in the inset), and (d) FFT patterns for  $\text{Co}_2(\text{OH})_2\text{CO}_3$ .

were clarified by using CV in the range of 0.01–3.0 V at a scan rate of 0.1 mV s<sup>-1</sup> (Figure 3a). Obviously, the first scan significantly differs from those of the following ones and an intense reduction peak ("1", at 0.76 V) is primarily ascribed to the formation of  $\text{LiOH}$ ,  $\text{Li}_2\text{CO}_3$  and solid electrolyte interphase (SEI) films,<sup>23,26</sup> which results from reaction 1 and the formation of SEI film. The irreversible peak labeled as "2" is attributed to reaction 2, which agrees well with the irreversible area of the peak labeled as "3". In the next anodic process, two broad oxidation peaks appear at 1.3 and 2.1 V. The former corresponds to reactions 2 and 3, and the latter is mainly due to the conversion reaction 1.<sup>25,32</sup> Peak "6" (0.83 V), which appears during the subsequent discharging process, seems to be nearly invariable and associated with reactions 2 and 3. However, peak "5" apparently moves to the lower voltage regions, which suggests that the original structure of  $\text{Co}_2(\text{OH})_2\text{CO}_3$  cannot be reversibly recovered after the first discharge process. This irreversible phenomenon is similar to that observed for  $\text{Co}_2(\text{OH})_3\text{Cl}$ .<sup>26</sup> Hence,  $\text{Co}_2(\text{OH})_2\text{CO}_3$  reacts with Li according to the following reactions:



The cycling performance of the as-prepared  $\text{Co}_2(\text{OH})_2\text{CO}_3$  was further investigated at 200 mA g<sup>-1</sup> (Figure 3b). The initial specific discharge and charge capacity are 1790 and 1190 mAh g<sup>-1</sup>, respectively, with low Coulombic efficiencies (CE) of 66.5%. The large irreversible capacity is attributed mainly to the formation of SEI at the electrode interface during the discharging process.<sup>33</sup> However, the discharge capacity decreases rapidly during the first 30 cycles and, thereafter, the capacity starts growing tardily, which is well documented in the previous reports and generally attributed to the reversible formation of a polymeric gel-like film originating from kinetic activation in the electrode.<sup>34,35</sup> Imposingly, after 100 cycles, the discharge capacity increases to 730 mAh g<sup>-1</sup>. Note that this capacity is much higher than that of pure  $\text{CoCO}_3$ ,<sup>36</sup> which

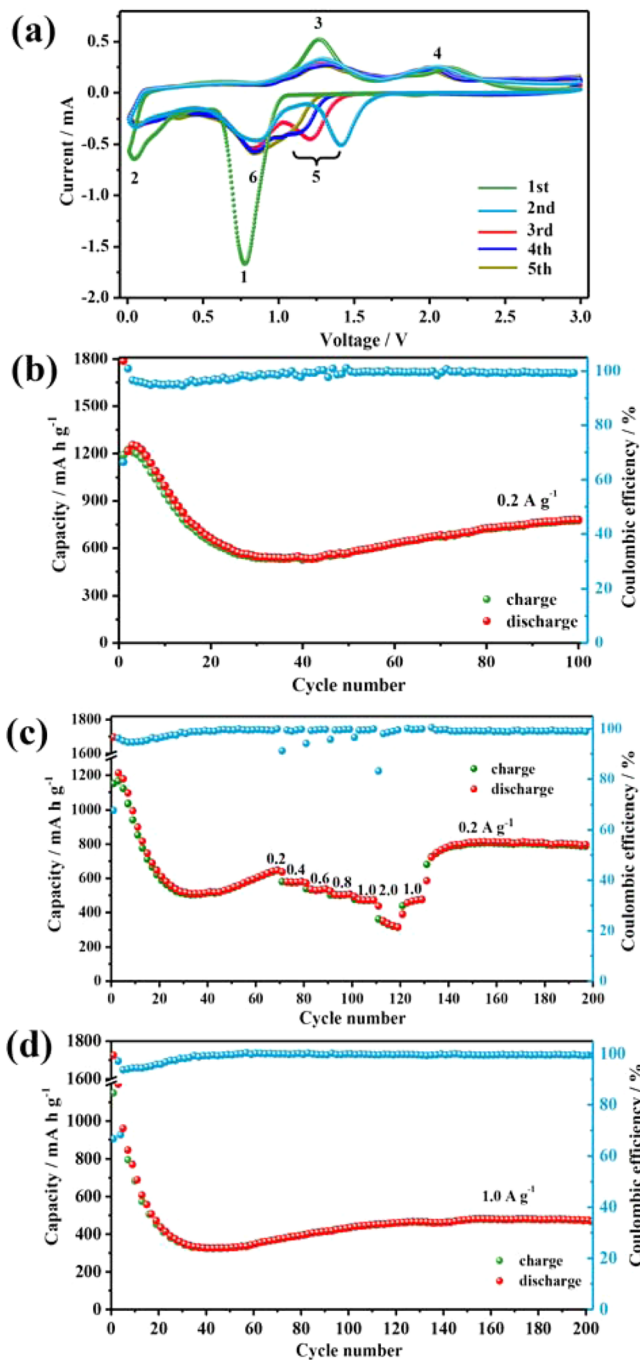


**Figure 3.** (a) CV curves of the  $\text{Co}_2(\text{OH})_2\text{CO}_3$  electrode; (b,c) cycling performance of the electrodes at  $0.2 \text{ A g}^{-1}$  and  $1.0 \text{ A g}^{-1}$ , along with Coulombic efficiency; and (d) rate performance of the  $\text{Co}_2(\text{OH})_2\text{CO}_3$  electrode.

stems from hydroxyl providing more lithium storage capacity.<sup>25</sup> More importantly, the CE after 30 cycles is close to 100% in the remanent battery operation, with regard to the reaction reversibility of the electrode. The electrode also shows long cycling stability under high current density. Galvanostatic charge–discharge tests involving 200 cycles were thus carried out at  $1 \text{ A g}^{-1}$  (Figure 3c). After activation at  $200 \text{ mA g}^{-1}$  in the first two cycles, the specific capacity presents the same trend as the previous description on cycling. First, it started to increase and the CE approaches 100% after 40 cycles, and then after cycling for 110 times, a specific capacity of  $400 \text{ mAh g}^{-1}$  still

remained without any decay. The result suggests high reversible capacity and good long-term cycle stability of  $\text{Co}_2(\text{OH})_2\text{CO}_3$ . Besides outstanding long-cycle stability, the  $\text{Co}_2(\text{OH})_2\text{CO}_3$  electrode also reveals excellent rate performance (Figure 3d). At  $200, 400, 600, 800, 1000$ , and  $2000 \text{ mA g}^{-1}$ , its discharge capacities are  $650, 571, 532, 500, 468$ , and  $323 \text{ mAh g}^{-1}$ , respectively. Importantly, when the current density returns to  $200 \text{ mA g}^{-1}$ , a discharge capacity of  $800 \text{ mAh g}^{-1}$  can be recovered, indicating the good rate performance of the electrode. Inspired by the results, an extended galvanostatic test was performed at the current density of  $200 \text{ mA g}^{-1}$ . A high reversible capacity of up to  $800 \text{ mAh g}^{-1}$  was maintained without any decay for over 60 cycles, suggesting the powerful lithium storage performance.

**Characterization and Electrochemical Measurements of CoO Nanonets.** Based on the TGA results,  $500 \text{ }^\circ\text{C}$  was chosen as the calcination temperature. The as-prepared CoO after thermal treatment was confirmed by XRD (Figure 4). The

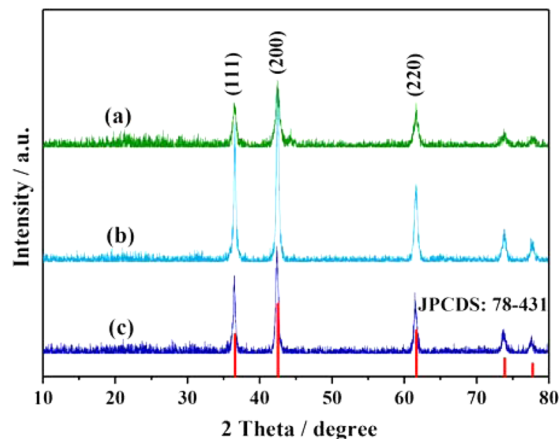


**Figure 4.** XRD patterns of CoO after thermal treatment at  $500 \text{ }^\circ\text{C}$  in Ar for different times of (a) 0 h, (b) 2 h, and (c) 4 h.

typical XRD pattern reveals that all reflection peaks can be well indexed to the cubic phase of CoO (JPCDS No. 78-431) and no impurity peaks can be identified, suggesting the complete phase transition from  $\text{Co}_2(\text{OH})_2\text{CO}_3$  to CoO. After simple thermal treatment in Ar, hierarchical structures composed of CoO nanosheets are produced, which was confirmed through FESEM. As seen in Figures 5a and 5b, various nanosheets with a thickness of  $\sim 50 \text{ nm}$  formed open hierarchical structure. Interestingly, the different nanosheets supported each other in various orientations and composed huge space. These nanosheets were closely embedded on the inter CoO and self-assembled to form hierarchical structure, which could prevent CoO from restacking and buffer local volume changes for LIBs on cycling. However, smaller nanosheets appear and the edge becomes less regular in Figure 5c. Therefore, the nanosheets would be gradually broken with increasing the heating time.

In order to clarify the morphology and microstructure of the as-synthesized CoO, TEM was also conducted. The low-resolution TEM images (Figures 6a–c) clearly show the nanonet nature of the resulting CoO, which is indeed composed of small interconnected porous nanosheets. As expected, thermal decomposition takes place during the calcination in Ar and generates gases such as  $\text{CO}_2$  and  $\text{H}_2\text{O}$ , which escape from  $\text{Co}_2(\text{OH})_2\text{CO}_3$  nanosheets, thus giving rise to the formation of highly porous CoO nanonets. The

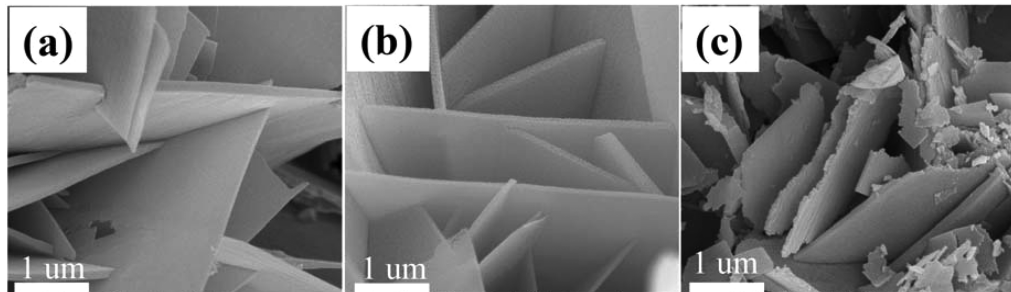


**Figure 5.** FESEM images of CoO samples obtained under different times: (a) 0 h, (b) 2 h, and (c) 4 h.

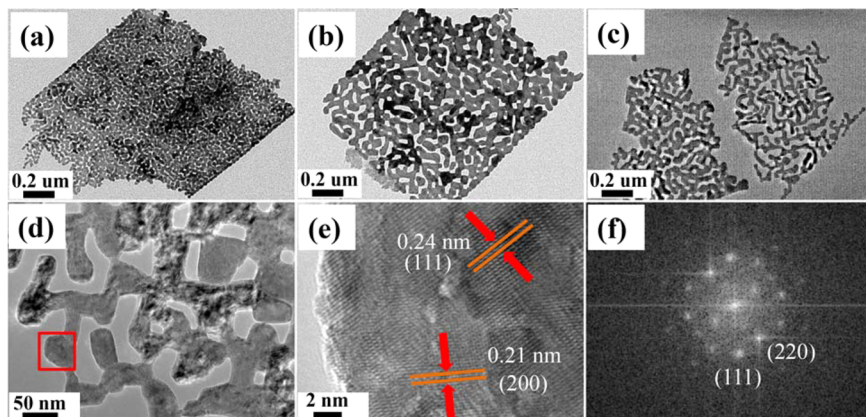
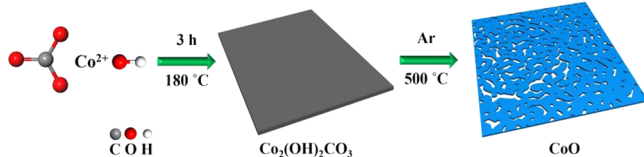


**Figure 6.** TEM images of the CoO samples obtained under different times: (a) 0 h, (b,d) 2 h, (c) 4 h, (e) HRTEM image, and (f) the corresponding FFT patterns for CoO-2.

fabrication from  $\text{Co}_2(\text{OH})_2\text{CO}_3$  to CoO is illustrated in Scheme 1. Note that the pore gradually enlarged with

#### Scheme 1. Schematic Illustration of Fabrication from $\text{Co}_2(\text{OH})_2\text{CO}_3$ Nanosheets to CoO Nanonets



prolonging the heating time. Compared with the complete nanonet in CoO-0, the nanonet in CoO-4 became cracked. [Here, the nomenclature format is given as CoO-A, where A denotes the heating time, in hours.] A magnified TEM image (Figure 6d) further reveals that the pores are composed of numerous interconnected nanoparticles. This appealing porous cross-linked feature is favorable for LIB anodes, because it can provide high active surface areas.<sup>37</sup> Compared with  $\text{Co}_2(\text{OH})_2\text{CO}_3$  nanosheets without any pores, the structure endows CoO with more lithium storage sites and large electrode–electrolyte contact area for high Li<sup>+</sup> flux across the interface. Moreover, this structure will lead to a higher capability for fast charge–discharge, provide extra free space to alleviate the structural strain, and accommodate the large volume variation associated with cycling, which give rise to improved cycling stability.<sup>38</sup> HRTEM analysis (Figure 6e) further demonstrates that the well-crystallized CoO displays clear lattice fringes. As observed, which is taken from the red square region in Figure 6d, the marked lattice fringes with *d*-spacings of 0.21 and 0.24 nm correspond to the (200) and

(111) interplane of CoO with cubic crystal structure, respectively. The fast Fourier transform (FFT) pattern of the lattice structure (Figure 6f) clearly indicates the nature of cubic CoO.

Electrochemical performances of CoO nanonets were also studied. CV was carried out to investigate the detailed electrochemical process under the same conditions as  $\text{Co}_2(\text{OH})_2\text{CO}_3$ . Evidently, there is significant difference between the first and following scan (Figure 7a). In the first cathodic scan, two distinct intense peaks located at ~0.70 and ~0.53 V are observed. The first peak corresponds to the formation of the SEI film, whereas the second peak was attributed to the initial reduction of CoO to Co and the formation of amorphous Li<sub>2</sub>O. However, the cathodic peak becomes weaker and shifts to ~1.25 V during the subsequent scans. The small shift may be due to structural reorganization, new phase formation, and polarization change in the electrode material.<sup>39</sup> Simultaneously, a broad peak located at ~2.1 V in the anodic scan curves can be attributed to the Li<sub>2</sub>O decomposition and the CoO regeneration. It is apparent that the CV curves of the second and three cycles overlap, indicating the excellent cyclic performance of CoO-2. To make a careful analysis on the cycling performance of the CoO electrodes, galvanostatic tests were evaluated at 1 A g<sup>-1</sup>. The results are given in Figure 7b, and the CoO electrodes show high capacity and excellent cycling stability. All can obtain capacities of more than 700 mAh g<sup>-1</sup> before 20 cycles. Although the capacity gradually decreases in the following cycling, stable capacities of 633, 558, and 440 mAh g<sup>-1</sup> after 200 cycles were still achieved, much higher than that of pure  $\text{Co}_2(\text{OH})_2\text{CO}_3$ . To the best of our knowledge, this carbon-free CoO-2 nanonets with highly porous frameworks are superior to those of previous reports

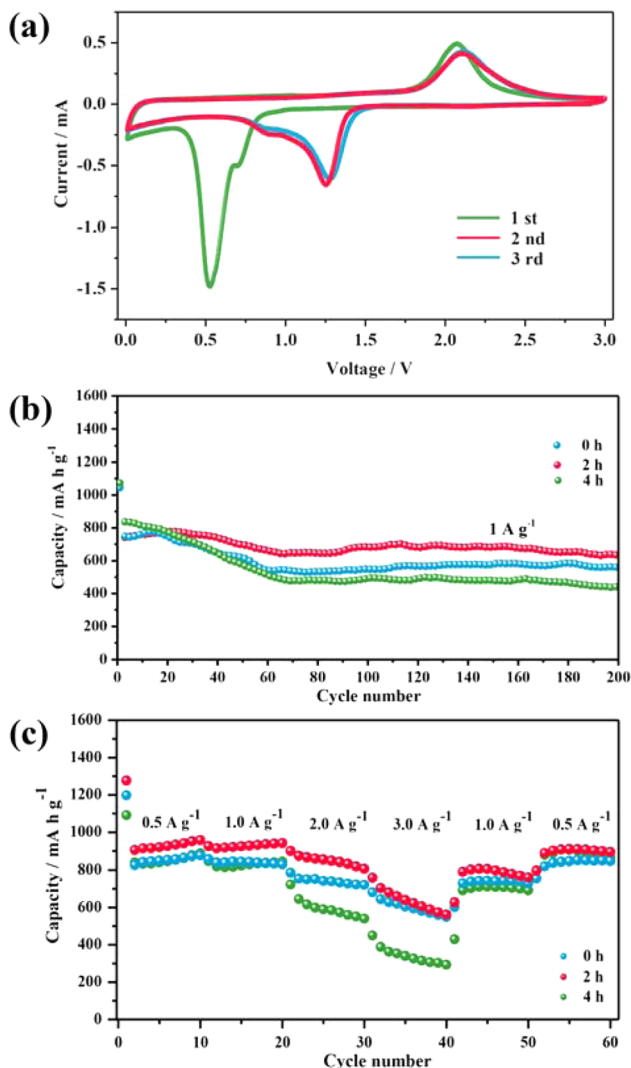


**Figure 7.** (a) CV curves of the CoO-2 electrode, (b) cycling performance at  $1.0 \text{ A g}^{-1}$ , and (c) rate performance of the CoO electrodes.

related to CoO or CoO/C composites.<sup>5,8–11,40</sup> In addition to the cycling stability, the CoO nanonets also display elevated rate performance. Figure 7c presents the rate capability from  $0.5 \text{ A g}^{-1}$  to  $3.0 \text{ A g}^{-1}$ . The sample CoO-2 displays reversible capacities of 958, 940, 810, and  $570 \text{ mAh g}^{-1}$  at  $0.5$ ,  $1$ ,  $2$ , and  $3 \text{ A g}^{-1}$ , respectively. These values are higher than those of CoO-0 and CoO-4, revealing the positive effects of the pore size. Note that the reversible capacities at  $0.5 \text{ A g}^{-1}$  are higher than

the theoretical value of CoO, which is due to the fact that the newly generated Co from CoO during the discharge process can activate or promote the reversible decomposition and formation of some SEI components.<sup>41</sup> More importantly, the capacity can recover to the initial level when the current is set back to  $0.5 \text{ A g}^{-1}$ , illustrating that the CoO nanonets have the good adaptability, which is attributed to the short lithium diffusion length benefiting from the extraordinary nanonets.

To investigate the reason why the CoO-2 nanonets delivered long-cycle stability, we collected TEM images of the three CoO electrodes cycled for 50 times at  $1.0 \text{ A g}^{-1}$  (Figure 8). Obviously, the highly porous nanonets of the CoO-2 powder was still maintained, even after repeated fast charging and discharging cycles, although the size of the pore has become smaller. This is because of the formation of amorphous  $\text{Li}_2\text{O}$  and of SEI film.<sup>42</sup> Compared with the integral CoO-2, the nanosheets of CoO-0 had cracked, and the nanonets of CoO-4 had been pulverized. Hence, the superior electrochemical properties for CoO-2 powders even at high current densities resulted from the rich moderate pores and structural stability.

**Influence of Pore Size on the High-Rate Performances of CoO.** CoO nanonets delivered different reversible capacities, and a possible explanation is that the high-rate performances of CoO rely on the pore size or specific surface area. Therefore, nitrogen adsorption–desorption analysis was conducted to confirm it (see Figure S1 in the Supporting Information). The Brunauer–Emmett–Teller (BET) specific surface area of samples CoO-0, CoO-2, and CoO-4 is  $30.5$ ,  $21.3$ , and  $16.1 \text{ m}^2 \text{ g}^{-1}$ ; the average pore size is  $15.2$ ,  $18.0$ , and  $23.5 \text{ nm}$ , respectively. Apparently, the high-rate performances of CoO-2 are associated with the pore size of nanonets. The shape of CoO-0 is the same as that of CoO-2 (see Figures 5a and 5b); however, the size pore is obviously different (see Figures 6a and 6b). Such small pores for CoO-0 could not provide enough space to accommodate the great change derived from the largely formed amorphous  $\text{Li}_2\text{O}$ , which results in the breakdown of the nanosheets and leads to capacity fading upon cycling (Figure 8a). Consequently, the capacity of CoO-0 is continuously reduced before 60 cycles. On the other hand, when the pore size is too large, nanonets will be bending during cycling,<sup>19</sup> which brings about the loss of electrical contact between the electrode materials with conductive additives. The electrode reaction for CoO depends on the simultaneous intercalation of  $\text{Li}^+$  and  $e^-$  into the active sites of a composite electrode.<sup>17</sup> However, the bending reduces the possibility of the combination of  $\text{Li}^+$  and  $e^-$ . More importantly, the newly generated interconnected Co networks during the discharge process would breakdown, which reduces the electron transfer and breaches the structural integrity of the nanonets (Figure

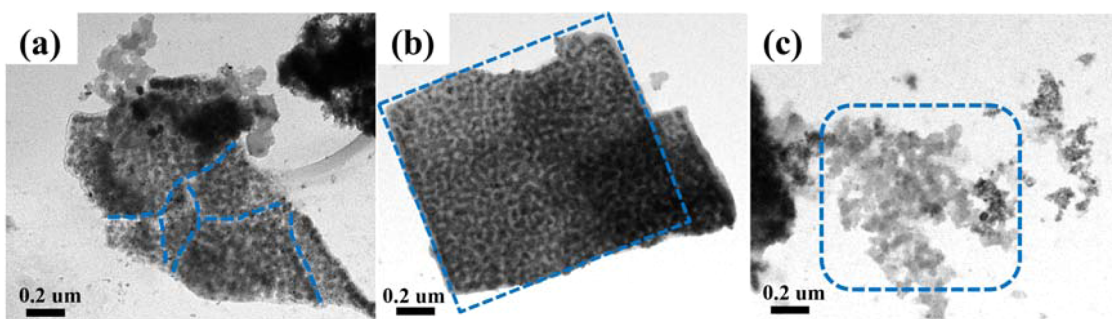


**Figure 8.** TEM images of the CoO samples at the fully charged state after 50 cycles at  $1 \text{ A g}^{-1}$ : (a)  $0 \text{ h}$ , (b)  $2 \text{ h}$ , and (c)  $4 \text{ h}$ .

8c).<sup>19</sup> In this scenario, CoO-4 exhibits lower specific capacity and more fast capacity fading than the other two samples (Figure 7b). Therefore, the electrochemical performance of the CoO-2 electrode can be attributed to the following reasons. First, the nanonets with optimum pore size provide enough void to contain the huge change and avoid bending of the nanonets to maintain the integrity of CoO nanonets. Second, a nanoporous metallic framework is comprised of the discharge produced cobalt nanoparticles, which inhibits pulverization (to allow extended charge–discharge cycles) and provides an electrical network (to enable high rate capability). Third, this porous structure not only increases active sites, but also reduces the diffusion distance for Li<sup>+</sup>, favorably allowing better reaction kinetics at the electrode surface.

## CONCLUSIONS

In summary, Co<sub>2</sub>(OH)<sub>2</sub>CO<sub>3</sub> nanosheets were prepared through an easy hydrothermal process, and initially studied as an anode material for Li ion batteries. Co<sub>2</sub>(OH)<sub>2</sub>CO<sub>3</sub> nanosheets exhibited impressive electrochemical performances including high capacity, stable power rate, and longevity. After sintering, the monoclinic Co<sub>2</sub>(OH)<sub>2</sub>CO<sub>3</sub> nanosheets were transformed into highly porous cubic CoO nanonets with more lithium storage sites, and shorter paths for both Li<sup>+</sup> and electron diffusion. Besides, the optimum-size pore could accommodate great volume change during cycling. Therefore, CoO nanonets exhibited greatly enhanced Li storage performances, including high reversible capacity and superior rate performance. More importantly, the highly porous CoO nanonets remained intact even after repeated fast charging and discharging cycles. Thereby, it is anticipated that Co<sub>2</sub>(OH)<sub>2</sub>CO<sub>3</sub> nanosheets and highly porous CoO nanonets are promising candidate materials for high-performance LIBs.

## ASSOCIATED CONTENT

### Supporting Information

More characterizations for Co<sub>2</sub>(OH)<sub>2</sub>CO<sub>3</sub> and CoO. The Supporting Information is available free of charge on the ACS Publications website at DOI: 10.1021/acsami.5b02152.

## AUTHOR INFORMATION

### Corresponding Author

\*E-mail: zhouchen@nankai.edu.cn.

### Notes

The authors declare no competing financial interest.

## ACKNOWLEDGMENTS

This work was supported by NSFC (No. 21421001) and MOE Innovation Team (No. IRT13022) in China.

## REFERENCES

- (1) Huang, X. K.; Cui, S. M.; Chang, J. B.; Hallac, P. B.; Fell, C. R.; Luo, Y. T.; Metz, B.; Jiang, J. W.; Hurley, P. T.; Chen, J. H. A Hierarchical Tin/Carbon Composite as an Anode for Lithium-Ion Batteries with a Long Cycle Life. *Angew. Chem., Int. Ed.* **2015**, *54*, 1490–1493.
- (2) Reddy, M. V.; Subba Rao, G. V.; Chowdari, B. V. Metal Oxides and Oxsalts as Anode Materials for Li Ion Batteries. *Chem. Rev.* **2013**, *113*, 5364–5457.
- (3) Sun, X. L.; Yan, C. L.; Chen, Y.; Si, W. P.; Deng, J. W.; Oswald, S.; Liu, L. F.; Schmidt, O. G. Three-Dimensionally “Curved” NiO Nanomembranes as Ultrahigh Rate Capability Anodes for Li-Ion

Batteries with Long Cycle Lifetimes. *Adv. Energy Mater.* **2014**, *4*, 1300912.

(4) Poizot, P.; Laruelle, S.; Grangeon, S.; Dupont, L.; Tarascon, J. Nano-Sized Transition-Metal Oxides as Negative-Electrode Materials for Lithium-Ion Batteries. *Nature* **2000**, *407*, 496–499.

(5) Xiong, S. L.; Chen, J. S.; Lou, X. W.; Zeng, H. C. Mesoporous Co<sub>3</sub>O<sub>4</sub> and CoO@C Topotactically Transformed from Chrysanthemum-Like Co(CO<sub>3</sub>)<sub>0.5</sub>(OH)·0.11H<sub>2</sub>O and their Lithium-Storage Properties. *Adv. Funct. Mater.* **2012**, *22*, 861–871.

(6) Peng, C. X.; Chen, B. D.; Qin, Y.; Yang, S. H.; Li, C. Z.; Zuo, Y. H.; Liu, S. Y.; Yang, J. H. Facile Ultrasonic Synthesis of CoO Quantum Dot/Graphene Nanosheet Composites with High Lithium Storage Capacity. *ACS Nano* **2012**, *6*, 1074–1081.

(7) Guan, X.; Nai, J. W.; Zhang, Y. P.; Wang, P. X.; Yang, J.; Zheng, L. R.; Zhang, J.; Guo, L. CoO Hollow Cube/Reduced Graphene Oxide Composites with Enhanced Lithium Storage Capability. *Chem. Mater.* **2014**, *26*, 5958–5964.

(8) Huang, X. L.; Wang, R. Z.; Xu, D.; Wang, Z. L.; Wang, H. G.; Xu, J. J.; Wu, Z.; Liu, Q. C.; Zhang, Y.; Zhang, X. B. Homogeneous CoO on Graphene for Binder-free and Ultralong-life Lithium Ion Batteries. *Adv. Funct. Mater.* **2013**, *23*, 4345–4353.

(9) Xie, K. W.; Wu, P.; Zhou, Y. Y.; Ye, Y.; Wang, H.; Tang, Y. W.; Zhou, Y. M.; Lu, T. H. Nitrogen-Doped Carbon-Wrapped Porous Single-Crystalline CoO Nanocubes for High-Performance Lithium Storage. *ACS Appl. Mater. Interfaces* **2014**, *6*, 10602–10607.

(10) Zhang, M.; Uchaker, E.; Hu, S.; Zhang, Q. F.; Wang, T. H.; Cao, G. Z.; Li, J. Y. CoO-Carbon Nanofiber Networks Prepared by Electrospinning as Binder-Free Anode Materials for Lithium-Ion Batteries with Enhanced Properties. *Nanoscale* **2013**, *5*, 12342–12349.

(11) Ryu, W. H.; Shin, J.; Jung, J. W.; Kim, I. D. Cobalt(II) Monoxide Nanoparticles Embedded in Porous Carbon Nanofibers as a Highly Reversible Conversion Reaction Anode for Li-Ion Batteries. *J. Mater. Chem. A* **2013**, *1*, 3239–3243.

(12) Hu, L.; Yan, N.; Chen, Q. W.; Zhang, P.; Zhong, H.; Zheng, X. R.; Li, Y.; Hu, X. Y. Fabrication Based on the Kirkendall Effect of Co<sub>3</sub>O<sub>4</sub> Porous Nanocages with Extraordinarily High Capacity for Lithium Storage. *Chem.—Eur. J.* **2012**, *18*, 8971–8977.

(13) Guan, H.; Wang, X.; Li, H. Q.; Zhi, C. Y.; Zhai, T. Y.; Bando, Y.; Golberg, D. CoO Octahedral Nanocages for High-Performance Lithium Ion Batteries. *Chem. Commun.* **2012**, *48*, 4878–4880.

(14) Li, D. D.; Ding, L. X.; Wang, S. Q.; Cai, D. D.; Wang, H. H. Ultrathin and Highly Ordered CoO Nanosheet Arrays for Lithium-Ion Batteries with High Cycle Stability and Rate Capability. *J. Mater. Chem. A* **2014**, *2*, 5625–5630.

(15) Liu, J. C.; Xu, Y. J.; Ma, X. J.; Feng, J. K.; Qian, Y. T.; Xiong, S. L. Multifunctional CoO@C Metasequoia Arrays for Enhanced Lithium Storage. *Nano Energy* **2014**, *7*, 52–62.

(16) Zhu, L. P.; Wen, Z.; Mei, W. M.; Li, Y. G.; Ye, Z. Z. Porous CoO Nanostructure Arrays Converted from Rhombic Co(OH)F and Needle-Like Co(CO<sub>3</sub>)<sub>0.5</sub>(OH)·0.11H<sub>2</sub>O and Their Electrochemical Properties. *J. Phys. Chem. C* **2013**, *117*, 20465–20473.

(17) Ren, Y.; Armstrong, A. R.; Jiao, F.; Bruce, P. G. Influence of Size on the Rate of Mesoporous Electrodes for Lithium Batteries. *J. Am. Chem. Soc.* **2010**, *132*, 996–1004.

(18) Lin, Z.; Yue, W.; Huang, D.; Hu, J.; Zhang, X.; Yuan, Z.-Y.; Yang, X. Pore Length Control of Mesoporous Co<sub>3</sub>O<sub>4</sub> and Its Influence on the Capacity of Porous Electrodes for Lithium-Ion Batteries. *RSC Adv.* **2012**, *2*, 1794–1797.

(19) Lin, F.; Nordlund, D.; Weng, T. C.; Zhu, Y.; Ban, C.; Richards, R. M.; Xin, H. L. Phase Evolution for Conversion Reaction Electrodes in Lithium-Ion Batteries. *Nat. Commun.* **2014**, *5*, 3358–3366.

(20) Kokubu, T.; Oaki, Y.; Hosono, E.; Zhou, H. S.; Imai, H. Biomimetic Solid-Solution Precursors of Metal Carbonate for Nanostructured Metal Oxides: MnO/Co and MnO–CoO Nanostructures and Their Electrochemical Properties. *Adv. Funct. Mater.* **2011**, *21*, 3673–3680.

(21) Wang, L. B.; Tang, W. J.; Jing, Y.; Su, L. W.; Zhou, Z. Do Transition Metal Carbonates Have Greater Lithium Storage Capability

- Than Oxides? A Case Study of Monodisperse  $\text{CoCO}_3$  and CoO Microspindles. *ACS Appl. Mater. Interfaces* **2014**, *6*, 12346–12352.
- (22) He, Y. S.; Bai, D. W.; Yang, X. W.; Chen, J.; Liao, X. Z.; Ma, Z. F. A  $\text{Co(OH)}_2$ -Graphene Nanosheets Composite as a High Performance Anode Material for Rechargeable Lithium Batteries. *Electrochim. Commun.* **2010**, *12*, 570–573.
- (23) Su, L. W.; Zhou, Z.; Qin, X.; Tang, Q.; Wu, D. H.; Shen, P. W.  $\text{CoCO}_3$  Submicrocube Graphene Composites with High Lithium Storage Capability. *Nano Energy* **2013**, *2*, 276–282.
- (24) Hu, Y. Y.; Liu, Z.; Nam, K. W.; Borkiewicz, O. J.; Cheng, J.; Hua, X.; Dunstan, M. T.; Yu, X.; Wiaderek, K. M.; Du, L. S.; Chapman, K. W.; Chupas, P. J.; Yang, X. Q.; Grey, C. P. Origin of Additional Capacities in Metal Oxide Lithium-Ion Battery Electrodes. *Nat. Mater.* **2013**, *12*, 1130–1136.
- (25) Park, G. D.; Ko, Y. N.; Kang, Y. C. Electrochemical Properties of Cobalt Hydroxylchloride Microspheres as a New Anode Material for Li-Ion Batteries. *Sci. Rep.* **2014**, *4*, 5785.
- (26) Zhong, Y. R.; Yang, M.; Zhou, X. L.; Luo, Y. T.; Wei, J. P.; Zhou, Z. Orderly-Packed Anodes for High-Power Lithium-Ion Batteries with Super Long Cycle Life: Rational Design of  $\text{MnCO}_3$ /Large-Area Graphene Composites. *Adv. Mater.* **2015**, *27*, 806–812.
- (27) Zhu, G. X.; Xi, C. Y.; Shen, M. Q.; Bao, C. L.; Zhu, J. Nanosheet-Based Hierarchical  $\text{Ni}_2(\text{CO}_3)(\text{OH})_2$  Microspheres with Weak Crystallinity for High-Performance Supercapacitor. *ACS Appl. Mater. Interfaces* **2014**, *6*, 17208–17214.
- (28) González López, J. *Envejecimiento De Carbonato Básico de Cobalto Amorfo en Disolución Acuosa a Temperatura Ambiente: Un Nuevo Método Para la Cristalización de  $\text{Co}_2\text{CO}_3(\text{OH})_2$  Precursor de  $\text{Co}_3\text{O}_4$* , <http://hdl.handle.net/10651/15142>, 2013.
- (29) Wang, S. L.; Qian, L. Q.; Xu, H.; Lü, G. L.; Dong, W. J.; Tang, W. H. Synthesis and Structural Characterization of Cobalt Hydroxide Carbonate Nanorods and Nanosheets. *J. Alloys Compd.* **2009**, *476*, 739–743.
- (30) Xu, R.; Zeng, H. C. Dimensional Control of Cobalt-Hydroxide-Carbonate Nanorods and Their Thermal Conversion to One-Dimensional Arrays of  $\text{Co}_3\text{O}_4$  Nanoparticles. *J. Phys. Chem. B* **2003**, *107*, 12643–12649.
- (31) Zhao, Z. G.; Geng, F. X.; Bai, J. B.; Cheng, H. M. Facile and Controlled Synthesis of 3D Nanorods-Based Urchinlike and Nanosheets-Based Flowerlike Cobalt Basic Salt Nanostructures. *J. Phys. Chem. C* **2007**, *111*, 3848–3852.
- (32) Ding, Z. J.; Yao, B.; Feng, J. K.; Zhang, J. X. Enhanced Rate Performance and Cycling Stability of A  $\text{CoCO}_3$ -Polypyrrole Composite for Lithium Ion Battery Anodes. *J. Mater. Chem. A* **2013**, *1*, 11200–11209.
- (33) Su, L. W.; Zhou, Z.; Shen, P. W. Ni/C Hierarchical Nanostructures with Ni Nanoparticles Highly Dispersed in N-Containing Carbon Nanosheets: Origin of Li Storage Capacity. *J. Phys. Chem. C* **2012**, *116*, 23974–23980.
- (34) Liu, W. W.; Lu, C. X.; Liang, K.; Tay, B. K. A High-Performance Anode Material for Li-Ion Batteries Based on a Vertically Aligned CNTs/ $\text{NiCo}_2\text{O}_4$  Core/Shell Structure. *Part. Part. Syst. Charact.* **2014**, *31*, 1151–1157.
- (35) Yuan, C. Z.; Zhang, L. H.; Hou, L. R.; Zhou, L.; Pang, G.; Lian, L. Scalable Room-Temperature Synthesis of Mesoporous Nanocrystalline  $\text{ZnMn}_2\text{O}_4$  with Enhanced Lithium Storage Properties for Lithium-Ion Batteries. *Chem.—Eur. J.* **2014**, *21*, 1262–1268.
- (36) Garakani, M. A.; Abouali, S.; Zhang, B.; Takagi, C. A.; Xu, Z. L.; Huang, J. Q.; Huang, J. Q.; Kim, J. K. Cobalt Carbonate and Cobalt Oxide/Graphene Aerogel Composite Anodes for High Performance Li-Ion Batteries. *ACS Appl. Mater. Interfaces* **2014**, *6*, 18971–18980.
- (37) Guan, C.; Wang, Y. D.; Zacharias, M.; Wang, J.; Fan, H. J. Atomic-Layer-Deposition Alumina induced Carbon on Porous  $\text{NiCo}_2\text{O}_4$  Nanonets for Enhanced Pseudocapacitive and Li-Ion Storage Performance. *Nanotechnology* **2015**, *26*, 014001.
- (38) Wang, Z. Y.; Zhou, L.; Lou, X. W. Metal Oxide Hollow Nanostructures for Lithium-Ion Batteries. *Adv. Mater.* **2012**, *24*, 1903–1911.
- (39) Hou, L. R.; Lian, L.; Zhang, L. H.; Pang, G.; Yuan, C. Z.; Zhang, X. G. Self-Sacrifice Template Fabrication of Hierarchical Mesoporous Bi-Component-Active  $\text{ZnO}/\text{ZnFe}_2\text{O}_4$  Sub-Microcubes as Superior Anode towards High-Performance Lithium-Ion Battery. *Adv. Funct. Mater.* **2015**, *25*, 238–246.
- (40) Liu, J.; Zhou, Y. C.; Liu, C. P.; Wang, J. B.; Pan, Y.; Xue, D. F. Self-assembled Porous Hierarchical-Like  $\text{CoO}@\text{C}$  Microsheets Transformed from Inorganic–Organic Precursors and their Lithium-Ion Battery Application. *CrystEngComm* **2012**, *14*, 2669–2674.
- (41) Su, L.; Zhong, Y.; Zhou, Z. Role of Transition Metal Nanoparticles in the Extra Lithium Storage Capacity of Transition Metal Oxides: A Case Study of Hierarchical Core–Shell  $\text{Fe}_3\text{O}_4@\text{C}$  and  $\text{Fe}@\text{C}$  Microspheres. *J. Mater. Chem. A* **2013**, *1*, 15158–15166.
- (42) Xu, G. L.; Li, J. T.; Huang, L.; Lin, W. F.; Sun, S. G. Synthesis of  $\text{Co}_3\text{O}_4$  Nano-Octahedra Enclosed By {111} Facets and their Excellent Lithium Storage Properties as Anode Material of Lithium Ion Batteries. *Nano Energy* **2013**, *2*, 394–402.